energies

Article

Variability in the Wind Spectrum between 10^{-2} Hz and 1 Hz

Neil Garcia, Biswaranjan Mohanty and Kim A. Stelson *

Department of Mechanical Engineering, University of Minnesota Twin Cities, Minneapolis, MN 55455, USA; garc0408@umn.edu (N.G.); mohan035@umn.edu (B.M.)
* Correspondence: kstelson@umn.edu

Abstract: Wind is an abundant, yet intermittent, source of renewable energy, with speeds changing both spatially and temporally over a wide range of time scales. While wind variability is well documented on large meteorological time scales and the behavior of turbulent flow at high frequencies is well understood, there remain questions in the literature regarding the intermediate region of these domains. Understanding wind variability at the microscale, here considering a frequency range of 10^{-2} Hz $< f <$ 1 Hz, is key for wind turbine control and modeling. In this paper, we quantify the variability of wind conditions for the meteorological tower at the Eolos wind research station in Minnesota using power spectral density analysis. Spectral analysis of wind samples with similar mean wind speeds was conducted to test the hypothesis that the wind spectrum's shape is independent of the mean wind speed. Historical wind speed data were compared and evaluated to identify diurnal, seasonal, and interannual trends in the spectrum of wind at frequencies above 10^{-3} Hz. We conclude that the shape of the wind spectrum is independent of the mean wind speed following the Kolmogorov $-5/3$ law for turbulent flows for incoming wind, with some variations in slope and spectrum magnitude. While no conclusive diurnal, seasonal, or interannual trends were observed, it is shown that some variations in both slope and spectrum magnitude can occur on these time scales.

Keywords: wind variability; turbulence spectrum; Kolmogorov $-5/3$ law; spectral analysis

Citation: Garcia, N.; Mohanty, B.; Stelson, K.A. Variability in the Wind Spectrum between 10^{-2} Hz and 1 Hz. *Energies* **2023**, *16*, 3701. https://doi.org/10.3390/en16093701

Academic Editor: Davide Astolfi

Received: 28 March 2023
Revised: 21 April 2023
Accepted: 24 April 2023
Published: 26 April 2023

1. Introduction

Wind power is an increasingly important tool in the global transition toward net-zero carbon emissions. However, the turbulent nature of wind creates challenges in the stability, predictability, modeling, and control of utility-scale wind turbines. Owing to the many meteorological factors that determine the weather, the variability of wind varies on a wide range of time scales [1]. Gusts of wind last for seconds to minutes. Day and night, and their associated temperature fluctuations, are bounded by the diurnal cycle. Seasonal variations dramatically change weather conditions in the temperate and frigid parts of the world. Climate change on an interannual scale drives extreme weather events. Such variability can be described through spectral analysis, which quantifies variability as a function of frequency using tools such as the power spectral density (PSD).

The spectrum of turbulent flows is not a new subject of study. Richardson first proposed the turbulent energy cascade process in 1922 [2]. In 1941, Kolmogorov related the turbulence spectrum to the energy cascade rate ε and the wavenumber k through dimensional analysis as

$$S(k) = C\varepsilon^{2/3}k^{-5/3} \tag{1}$$

where $S(k)$ is the PSD of streamwise velocity fluctuations u'. This relationship is known as the Kolmogorov $-5/3$ law. Note that k is directly related to frequency f as

$$k = \frac{f}{v_p} \tag{2}$$

where v_p is the phase velocity; for clarity and relevance to the present study, the term "wind spectrum" will henceforth refer to the PSD of u' as a function of f, or $S(f)$. The consequence of (1) and (2) is that $S(f)$ is expected to fall off at a constant slope of $-5/3$ when plotted on a log–log scale [3]. Classical studies of the frequency content of turbulent flows by Kaimal and Grant are consistent with the Kolmogorov $-5/3$ law [4,5]. Constant C was found to be ~1.5 for all turbulent flows [6]. However, experimental studies of turbulence spectra in pipe flows have demonstrated that the location of the spectral peak varies at high Reynolds numbers [7].

The literature generally cites the Kolmogorov $-5/3$ law when characterizing the wind spectrum, but our understanding of the broader wind spectrum and the atmospheric boundary layer has grown over the past century. A 1956 study by Van der Hoven was one of the foundational works on wind spectral analysis, describing methods for estimating spectra over wide frequency ranges and producing a wind spectrum covering frequencies from 0.0007 to 900 cycles/h (~2×10^{-7} Hz to 0.25 Hz) [8]. His identification of a spectral peak at 1 min^{-1} (~1.67×10^{-2} Hz) motivated the frequency range of $f > 10^{-2}$ Hz to be studied in this work, henceforth referred to as the "microscale" wind spectrum. This definition of "microscale" is consistent with the atmospheric scale definitions given by Orlanski in 1975 [9], Pielke in 1984 [10], and Stull in 1988 [11], summarized by Thunis and Bornstein in 1995 [12]. A 1961 study by Davenport presented similar horizontal spectra recorded at various locations and elevations [13]. A 1962 study by MacCready and a 1966 study by Payne and Lumley examined the validity of Kolmogorov's theory in atmospheric flows [14,15]. A 2002 study by Högstrom et al. examined detached large eddies in atmospheric flows at low elevations and their effects on the wind spectrum [16]. A 2016 study by Larsén et al. revisited the full-scale spectrum of boundary layer winds to better understand the mesoscale and microscale wind spectrum as it varied in space [17]. A 2019 study by Wang et al. investigated Kolmogorov's theory for the airflow above the ocean and its interactions with ocean surface waves [18].

More recent advancements in wind farm technology have spurred interest in the microscale frequency content of wind for use in advanced control strategies and wind farm computer models. Owing to the time-varying nature of wind, wind turbines must employ control strategies to evaluate the current operating conditions and change turbine behavior to maximize power capture at any given time. It is difficult to measure and use wind speed measurements in real time. Wind speed measurement can be avoided by using one of the most common methods for wind turbine control, the $K\omega^2$ law, also known as torque control [19]. This method seeks to match generator torque τ_c as

$$\tau_c = K\omega^2 \tag{3}$$

where ω is the rotor speed. K is given as

$$K = \frac{1}{2}\rho\pi R^5 \frac{C_{p,max}}{\lambda_*^3} \tag{4}$$

where ρ is the density of air, R is the rotor radius, and λ_* is the tip–speed ratio associated with the maximum power coefficient $C_{p,max}$. This approach depends on having an accurate value of K [20]. Modeling errors and machine wear change the control parameters and decrease the overall efficiency. To combat this problem, maximum power point tracking (MPPT) control strategies are designed to adapt K.

The two most popular MPPT control strategies to find the most accurate value of K are hill climbing search (HCS) and extremum seeking control (ESC) [19,21,22]. Both HCS and ESC operate on the same principle: varying a control variable to produce an observable response in the objective function, in this case, power. HCS uses a variable step size and ESC uses a low-amplitude dither signal to vary the control variable. In both cases, the resulting response provides information about the direction in which the control variable should be changed to approach the maximum power point.

The appropriate amplitude of these disturbances has been the subject of much research, but the frequency at which these control strategies perturb the control variable is also critical [22–24]. If the disturbance frequency is too low, the controller will be too slow, but if the disturbance frequency is too high, the controller will respond to unwanted noise. A better understanding of the frequency content of wind will inform the design of MPPT controllers. Previous studies using extremum seeking control identified appropriate dither frequencies of 0.008 Hz and 0.013 Hz for the National Renewable Energy Laboratory (NREL) 600 kW CART3 turbine [20,25]. Previous studies conducted by the Hydraulic Power Transmission Laboratory at the University of Minnesota explored MPPT controllers in a 60 kW turbine using a dither frequency of 0.011 Hz [26–28], and an ongoing study by the lab has identified an appropriate controller bandwidth of 0.033–0.073 Hz [29].

The computer models used to predict and optimize the behavior of wind turbines require knowledge of $S(f)$ [30]. Actively developing codes for turbine characterization and simulation, such as NREL's OpenFAST [31] and TU Berlin's QBlade [32], use information about the wind spectrum to model inflow conditions. NREL's TurbSim is one of the most popular tools used to generate simulated wind fields [33]. Rather than using a fluid mechanics-based simulation, TurbSim uses spectra of velocity in the frequency domain and converts them to a time-varying velocity profile through inverse Fourier transformation. Users can provide their own spectra or choose from preexisting standard spectra based on IEC 61400-1 standards [34]

$$S_1(f) = 0.05{\sigma_1}^2(\Lambda_1/V_{hub})^{-2/3}f^{-5/3} \tag{5}$$

$$S_2(f) = S_3(f) = \frac{4}{3}S_1(f) \tag{6}$$

where indices 1, 2, and 3 indicate streamwise, crosswise, and vertical components, σ_1 is the turbulence standard deviation, and Λ_1 is the streamwise turbulence scale parameter. Note the $f^{-5/3}$ term in (5), which reflects the Kolmogorov $-5/3$ law. OpenFAST and QBlade use the flow field to predict the response turbine behavior, such as power performance and blade loading. A better understanding of the wind spectrum opens the door for the further development of such statistical wind models.

Using large sets of high-resolution wind data, the characteristics of the wind spectrum at the microscale frequency range and its variability over larger time scales can be calculated to test the hypothesis that microscale wind spectra are independent of meteorological changes over large time scales, as Van der Hoven and Larsén et al. asserted. To better inform control strategies and models for wind farms, answers to the following questions are sought:

- Is the wind spectrum at microscale frequencies independent of the mean wind speed?
- How does the microscale wind spectrum change over diurnal, seasonal, and interannual time scales?
- Is the Kolmogorov $-5/3$ law an appropriate model for the microscale wind spectrum?

2. Methods

2.1. Experimental Setup

The Eolos wind research station, part of the University of Minnesota's St. Anthony Falls Laboratory, has been collecting 1 Hz wind data using its onsite met tower since its completion in January 2012 [35] and has supported several wind power studies [36–45]. The wind research station is located at the University of Minnesota Outreach Research and Education (UMore) Park, Rosemount, MN (44 43.693, −93 2.8858). The site is characteristic of the American Midwest—surrounded by farmland and not near any major bodies of water. A labeled satellite image of the site is shown in Figure 1a.

(**a**) (**b**)

Figure 1. (**a**) Satellite rendering and overlaid compass rose of the Eolos wind research station at the University of Minnesota Outreach Research and Education (UMore) Park, Rosemount, MN. Google Maps. (**b**) Scale diagram of the Eolos wind research station. Diamonds represent sonic anemometers. Circles represent other sensors.

The wind research station is equipped with a Clipper Liberty 2.5 MW turbine [46] with a rotor diameter of 96 m and a hub height of 80 m. The turbine's Supervisory Control and Data Acquisition System (SCADA) is instrumented to record wind speed, wind direction, ambient temperature, and air density at hub height at 1 Hz.

A 130 m met tower is located 160 m upstream (due south) of the turbine, within the International Electrotechnical Commission (IEC) recommended distance of 2 rotor diameters [35]. High-resolution CSAT3 3D sonic anemometers with a sampling rate of 20 Hz are attached to the tower with 6 m booms, custom designed to limit sway and ensure accurate measurements [43]. Anemometers are mounted at 4 key elevations, chosen based on the boundaries of the rotor swept area, hub height, mid-span of blades, and a common height for comparison with other meteorological data. Additional 1 Hz cup anemometers, wind vanes, and air temperature and relative humidity sensors are mounted at the same key elevations and 2 additional key elevations. A scale diagram of the met tower and turbine with key dimensions labeled is shown in Figure 1b.

2.2. Data Collection

Preliminary spectral analysis using data collected at the turbine hub was conducted at the start of the study. However, turbulence around the hub caused by the turbine rotor rotation created artificial peaks at the harmonics of the rotor speed. Therefore, the data used for this study were sourced from the sonic anemometers of the met tower. The sonic anemometer mounted at 127.9 m was chosen for consistency with Van der Hoven (125 m), Davenport (153 m), and Larsén et al. (100 m). The turbulence intensity at 127.9 m at this site was previously measured to be 0.115 [43]. The integral length scale at this site was previously recorded between 3.4 m and 14.6 m [47].

Data were collected in four batches, to be analyzed separately. The preliminary data batch is a single 7-day data set taken in May 2021. May was chosen as the month of interest because wind speed maxima in the north–central United States are expected to occur in the springtime [1], and May 2021 was chosen for its large amount of usable data (discussed below). The remaining three batches of data sets were chosen according to the large time scales of interest. For diurnal variation, eight 2 h data sets (four from 11 a.m.–1 p.m. and four from 11 p.m.–1 a.m. the next day) were taken from four consecutive days in May 2021 (part of the same preliminary 7-day data set). For seasonal variation, one 7-day data set was taken from each month in 2021. For interannual variation, one 7-day data set was taken from each May from 2012 to 2021.

2.3. Pre-Processing

The components of wind speed moving north to south and west to east, U_N and U_W, are collected at 20 Hz by the met tower sonic anemometer and averaged to 1 Hz readings. The wind speed magnitude was calculated as

$$U = \left|\vec{U}\right| = \sqrt{{U_N}^2 + {U_W}^2} \tag{7}$$

Sensor errors were trimmed from the data by inspection. The constraint $C_1 : U_N \leq 0$ was imposed on the data. This removed any influence from turbine wake when the met tower was downstream of the turbine, as the prevailing wind direction was south to north. The gaps created by this constraint produced several smaller subsets of valid wind data on the scale of seconds to minutes to use for analysis. Subsets too small for frequency analysis in the frequency range of interest (point count $n < 32$ for Section 3 and $n < 512$ for Section 4) were removed. The remaining subsets of data will be referred to as U_{data}.

Note that the fraction of usable data varied between data sets (particularly in Section 4) due to sensor errors, etc., and was sometimes lower than that discussed in previous works [17]. However, these data sets were retained to best capture spectral changes over consecutive time periods, which was a primary objective of this study. These data sets are called out explicitly in Section 4.

3. Frequency Content across Mean Velocities Using Wind Bins

3.1. Analysis

A plot of U_{data} from the May 2021 data set is shown in Figure 2a. After imposing C_1 and the subset size requirement, 81.6% of the data qualified as U_{data}, broken into 376 subsets. A wind rose of U_{data} is shown in Figure 2b. U_{data} had a median turbulence intensity of 0.241 and a median integral length scale of 13.8921, calculated following the procedure described in [1].

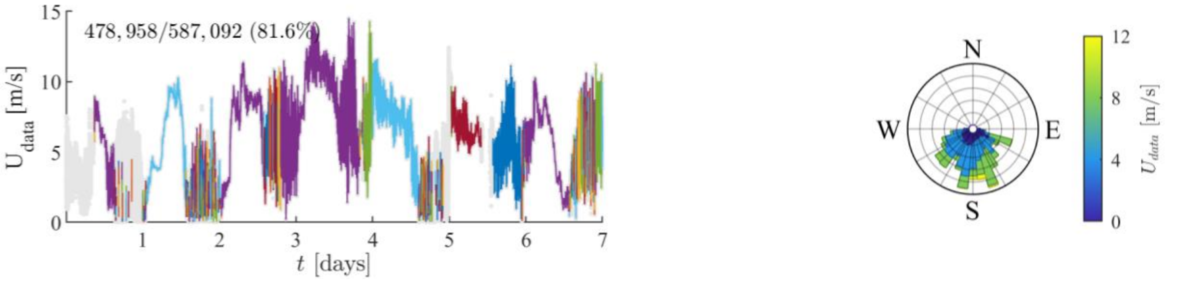

(**a**) (**b**)

Figure 2. (**a**) Wind speed over time. Colored data U_{data} satisfy the direction and subset size requirements. Each color represents a different subset. (**b**) Wind rose of U_{data}.

To check the quality of the data set, a probability density function (PDF) of U_{data} was produced and is shown in Figure 3a. The distributions of wind speeds are typically characterized by the Weibull distribution

$$p(U)dU = \frac{B}{A}\left(\frac{U}{A}\right)^{B-1} exp\left(-\left(\frac{U}{A}\right)^{B}\right)dU \tag{8}$$

where A is the scale factor and B is the shape factor. The shape factor provides information about the variability of wind over the whole data set. A lower shape factor implies greater variations in wind speed. U_{data} does not closely fit a Weibull distribution; the distribution is bimodal, with the main peak skewed right. However, the PDF does agree well with PDFs found in the literature for the same height and geographic region [48].

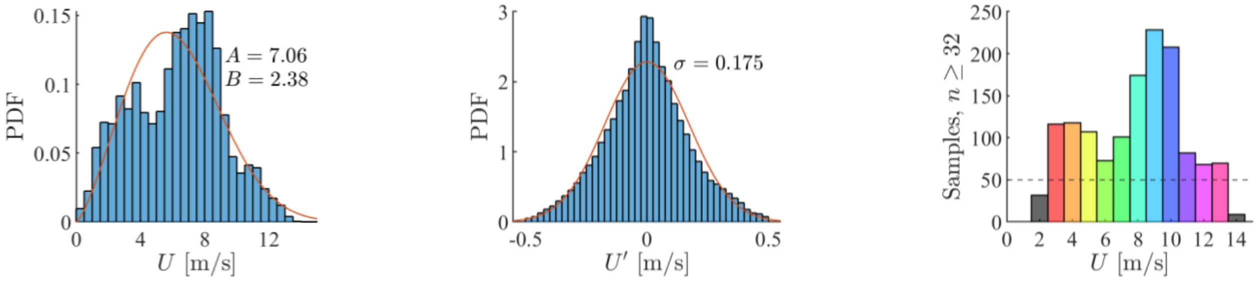

(**a**) (**b**) (**c**)

Figure 3. (**a**) Probability density function (PDF) of U. Red line shows the best-fit Weibull distribution. (**b**) PDF of U'. Red line shows the best-fit Gaussian distribution. (**c**) Histogram showing the number of samples with points $n \geq 32$ per bin. Colors for reference in Figures 4 and 5.

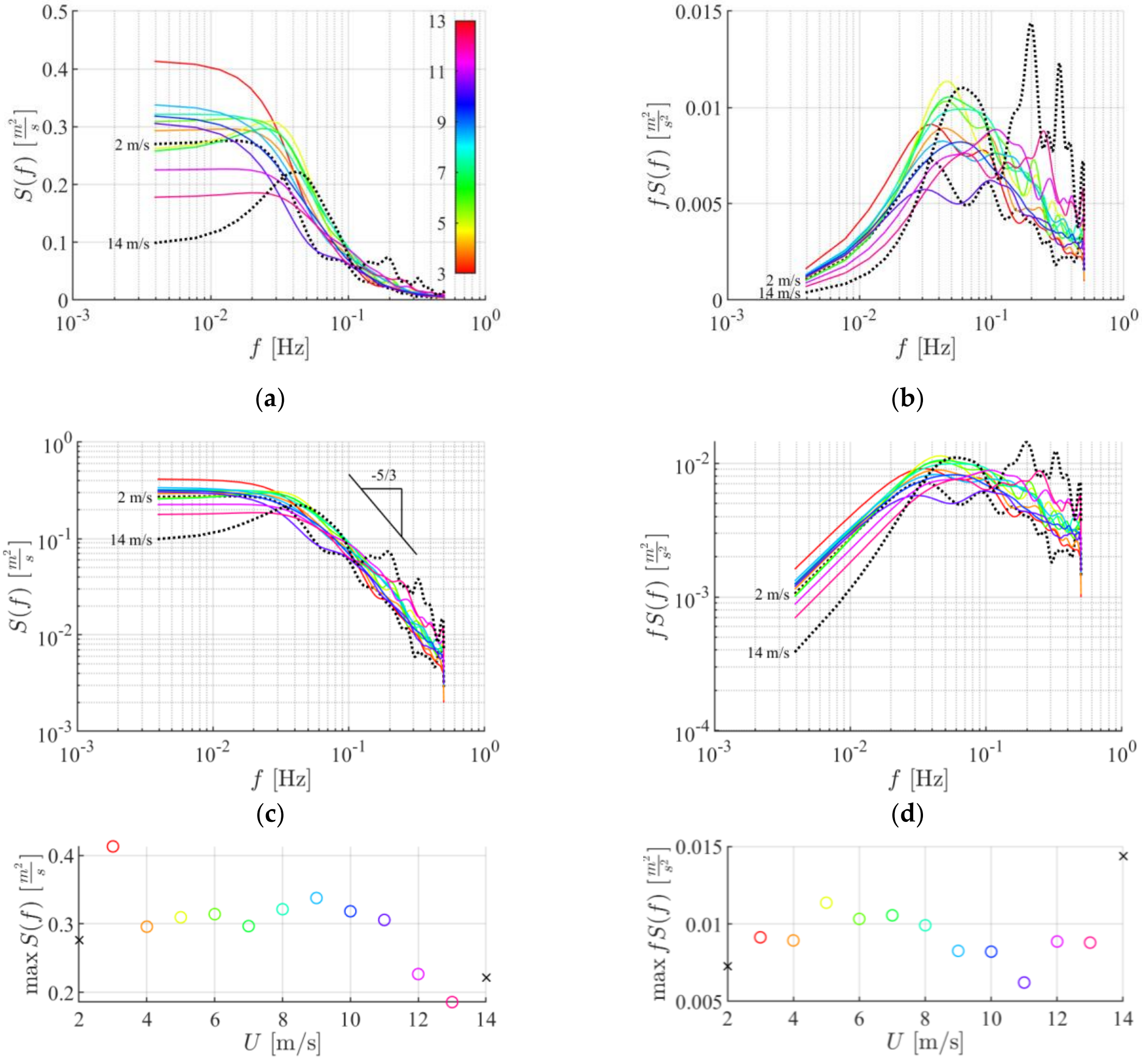

(**a**) (**b**)

(**c**) (**d**)

(**e**) (**f**)

Figure 4. (**a**) $S_{bin}(f)$ on a semilog scale. Spectra for bins with low sample counts are plotted as dashed lines. (**b**) $fS_{bin}(f)$ on a semilog scale. (**c**) $S_{bin}(f)$ on a log–log scale. (**d**) $fS_{bin}(f)$ on a log–log scale. (**e**) Maximum values of $S_{bin}(f)$. (**f**) Maximum values of $fS_{bin}(f)$.

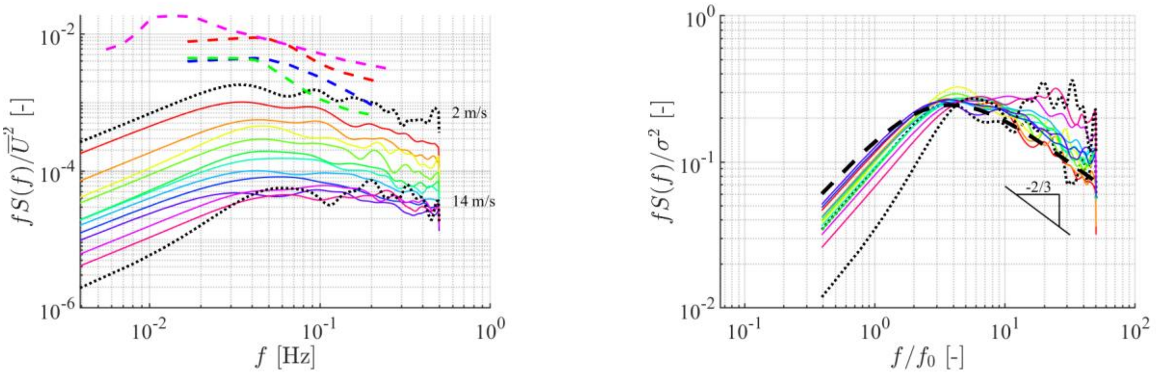

(**a**) (**b**)

Figure 5. (**a**) Spectra nondimensionalized by $\overline{U}$. Red, blue, and green dashed lines are 12.2 m, 64 m, and 153 m spectra adapted from Davenport [4]. Magenta dashed line adapted from Van der Hoven [8]. (**b**) Spectra nondimensionalized by σ^2. Dashed line adapted from Kaimal et al. [4].

Low-frequency contributions to the spectrum are undesirable when investigating the high-frequency content of the spectrum [1]. These two components can be separated through Reynolds decomposition, which yields mean velocities $\overline{U}$ and fluctuations about the mean U' as

$$U = \overline{U} + U' \tag{9}$$

A similar quality check was carried out for wind fluctuations, and a PDF of U' is shown in Figure 3b. The distributions of wind speed fluctuations are typically characterized by the Gaussian (normal) distribution, dictated by mean value μ and standard deviation σ. The data set agrees fairly well with the Gaussian distribution and with PDFs found in the literature for the same height and geographic region [48].

Each of the subsets was broken into smaller samples according to wind speed bins to ensure stationarity during analysis. A second constraint $C_2 : U \in [U_1, U_2]$ was imposed on the data, where U_1 and U_2 are integers bounding each bin. Samples too small for frequency analysis were removed. A histogram showing the distribution of binned U_{data} samples is shown in Figure 3c. Bins with fewer than 50 valid samples are plotted in black.

Each sample was analyzed separately using Welch's PSD estimate with a window size of $N = 32$ points. A window size of N = 32 points was chosen as a power of 2 for Welch's PSD estimate to accurately capture frequencies as slow as (32 s)$^{-1}$ = 0.0078 Hz < 0.01 Hz. Using a window size of the next highest power of 2, 64 points, would severely limit the number of usable samples. The number of discrete Fourier transform (DFT) points was 256, or the next power of 2 greater than the length of the sample. The resulting spectra were averaged over all subsets as recommended in [1], producing one average spectrum $S_{bin}(f)$ for each bin.

3.2. Results and Discussion

$S_{bin}(f)$ and $fS_{bin}(f)$ are plotted in Figure 4 on both semilog and log–log scales. Plots of $fS(f)$ can be used to calculate variance contributions over a given frequency range [8] and help to visualize where declines in $S(f)$ begin. The peaks in the plot of $fS_{bin}(f)$ show the frequency at which $S_{bin}(f)$ began to fall off. Spectra with low sample counts (<50 samples) were plotted as dotted lines. Maximum values of $S_{bin}(f)$ and $fS_{bin}(f)$ for each bin were plotted to check for the dependence of low-frequency content and spectral peaks on mean wind speed. The colors correspond to the bins shown in Figure 3c. Spectra nondimensionalized by mean wind speed $\overline{U}$ and variance σ^2 are presented in Figure 5 and compared with spectra from the literature. In Figure 5b, f_0 = 10^{-2} is defined as the approximate intercept of the extrapolated subrange spectrum, where $fS_{bin}(f)/\sigma^2 = 1$ [13].

$S_{bin}(f)$ for sufficiently sampled bins had a consistent shape at lower frequencies across bins, with more noise above 4×10^{-2} Hz. The maximum magnitude of $S_{bin}(f)$ at low frequencies tended to drop off as wind speed increased, although this trend was less clear for moderate wind speeds. $S_{bin}(f)$ agreed well with the Kolmogorov $-5/3$ law across all bins and was consistent with existing wind spectra from the Eolos wind station [32].

$fS_{bin}(f)$ for sufficiently sampled bins had a consistent general shape at lower frequencies across bins, with more variation in shape across bins above 4×10^{-2} Hz. The peak magnitude of $fS_{bin}(f)$ did not have a strong dependence on wind speed. However, the frequency at which the peak occurred did depend on wind speed. Peaks tended toward higher frequencies as the wind speed increased. Significant noise in $fS_{bin}(f)$ in the frequency range above 7×10^{-2} Hz made it difficult to explore this further; more samples are likely required.

Davenport reported plateaus in $fS(f)/\overline{U}^2$ that began to drop off at 5×10^{-2} Hz for all three elevations (12.2 m, 64 m, and 153 m), which roughly agreed with the frequencies observed in this study [13]. Spectra were nondimensionalized by $\overline{U}$ = (16.5, 20.7, 25.0) m/s. All three dimensionless spectra from Davenport had higher magnitudes than those recorded in this study. Van der Hoven predicted a peak in $fS(f)$ at ~1.4×10^{-2} Hz, a lower frequency than that observed here [8]. The spectrum was nondimensionalized by $\overline{U}$ = 13 m/s. Larsén et al. did not provide a characteristic velocity with which to nondimensionalize and thus were omitted from Figure 5 [17]. $fS_{bin}(f)$ generally agreed with the spectra observed by Larsén et al., though their spectra had less pronounced peaks at similar elevations [17]. $fS_{bin}(f)/\sigma^2$ had excellent agreement with the spectra presented by Kaimal et al. [4].

The spectra for bins with low sample counts were noisy and inconsistent. $S_{bin}(f)$ most clearly departed from the rest of the spectra at low frequencies, and $fS_{bin}(f)$ most clearly departed from the rest of the spectra at high frequencies. We expect that, with more data, all bins will follow the same trends.

As $\overline{U}$ increased, variability in U' increased above ~4×10^{-2} Hz and decreased below ~4×10^{-2} Hz. The location of peaks in $fS_{bin}(f)$ and the corners in plots of $S_{bin}(f)$ marked the start of the inertial subrange. The extent of the inertial subrange, therefore, shrank (starting at higher frequencies) as the wind speed increased. We conclude that, while the shape of the wind spectrum was independent of the mean wind speed, the magnitude of the spectrum of wind speed was not independent of the mean wind speed. These results agree with the conclusions drawn for high-Reynolds-number pipe flows discussed in [7].

4. Changes in Variability across Large Time Scales

4.1. Analysis

The same pre-processing steps were followed using the diurnal, seasonal, and interannual data batches, but the data were not broken into bins, yielding larger subsets for analysis. Using the mean velocity of full, unbroken subsets preserved low-frequency variability outside of the frequency range of interest. To avoid this, a centered moving average U_{mov} was used to calculate U' at each time step i. A window size of N = 512 points was chosen for the moving average for consistency with Welch's PSD estimate (see below). U' was then calculated for each time step i as

$$U'_i = U_i - \overline{U}_{mov,i} \tag{10}$$

The spectrum of U' was then estimated for each subset using Welch's PSD estimate with a window size of 512. A window size of N = 512 points was chosen to accurately capture frequencies as slow as $(512 \text{ s}/4)^{-1} = 0.0078$ Hz < 0.01 Hz. Note that, here, we increased N to more accurately capture the frequency range of interest, given that the sample size was no longer constrained by bins. The number of DFT points was 256, or the next power of 2 greater than the length of the subset. The resulting spectra can be characterized as a power function in the form

$$S(f) = af^p \tag{11}$$

which forms a line on a log–log plot, where a is the intercept with $x = 10^0 = 1$ and p is the line's slope.

4.2. Figures

Wind roses of U_{data} for each data batch are shown in Figure 6 for reference. Figures 7–9 show the PSD of each data batch $S(f)$ on a log–log scale. Plots of a, p, and max S were plotted to show changes in the spectrum over time. Note $S = S(f)$. The means of U'_{data} μ and standard deviation of U_{data} σ, as well as shape factor of U_{data} B, were plotted for reference. These five parameters will be referred to as the spread parameters.

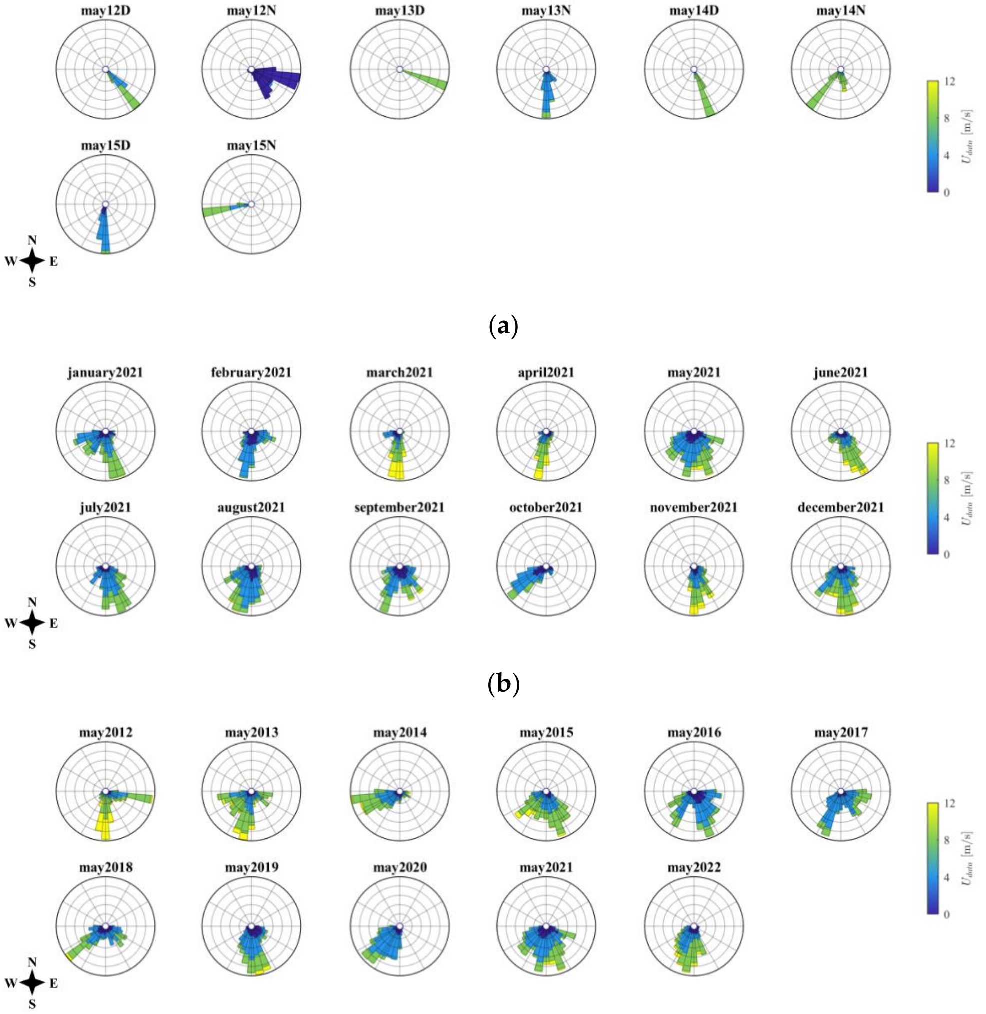

(**a**)

(**b**)

(**c**)

Figure 6. (**a**) Wind roses of U_{data} for the diurnal data batch. (**b**) Wind roses of U_{data} for the seasonal data batch. (**c**) Wind roses of U_{data} for the interannual data batch.

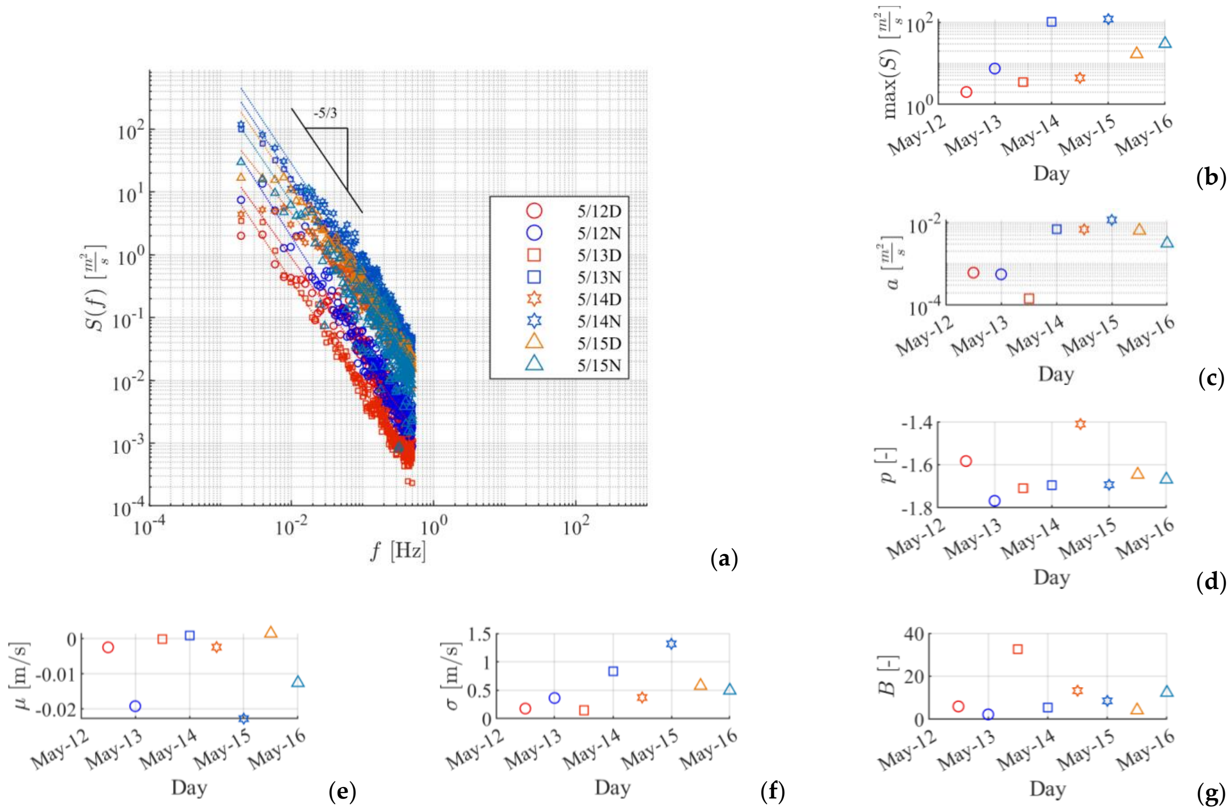

Figure 7. (**a**) Power spectra of the diurnal data batch, with best-fit lines in log–log space. −5/3 slope plotted as black line. (**b**–**g**) Plots of spectral characteristics and spread parameters over time.

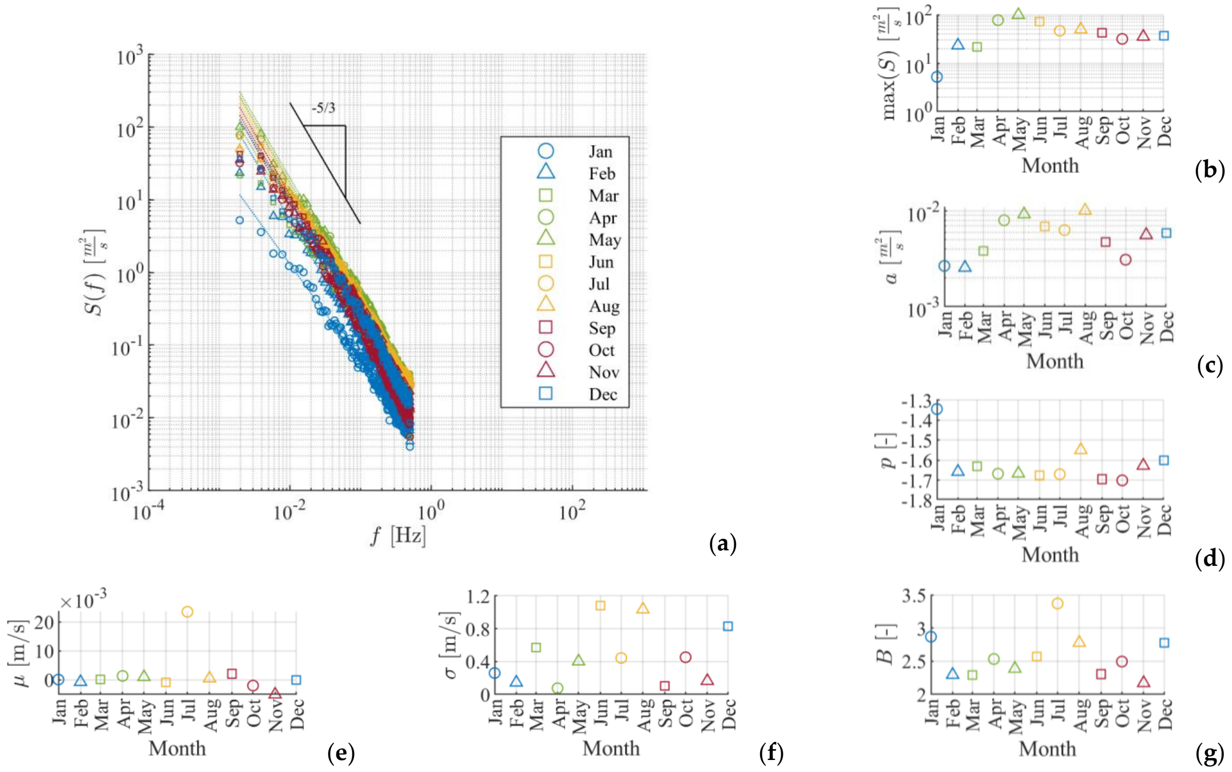

Figure 8. (**a**) Power spectra of the seasonal data batch, with best-fit lines in log-log space; −5/3 slope plotted as black line. (**b**–**g**) Plots of spectral characteristics and spread parameters over time.

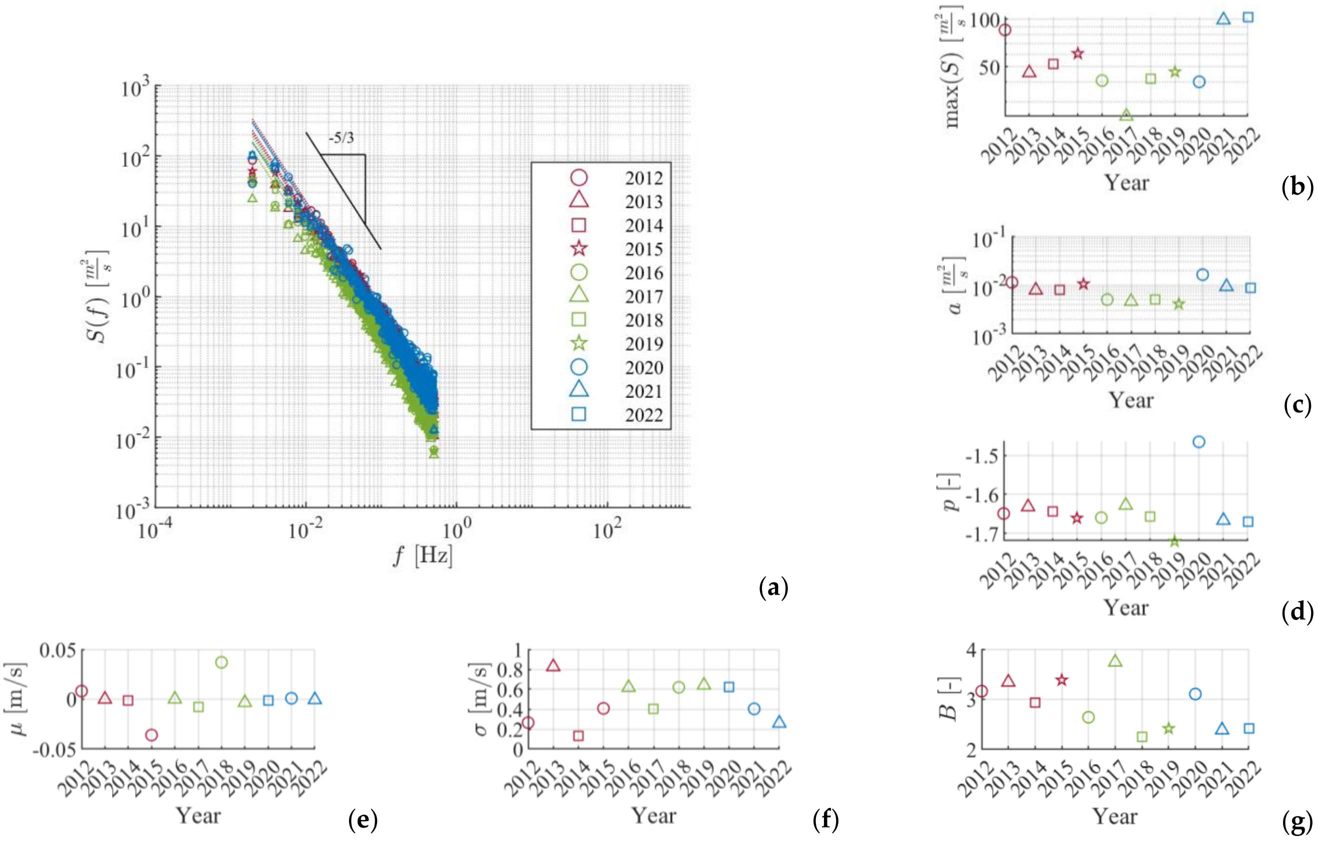

Figure 9. (**a**) Power spectra of the interannual data batch, with best-fit lines in log–log space; −5/3 slope plotted as black line. (**b**–**g**) Plots of spectral characteristics and spread parameters over time.

4.3. Diurnal Results and Discussion

At least 90% of the data of all 2 h data sets satisfied the conditions for U_{data}, except for the nighttime 12 May data set (59.6%) and the nighttime 15 May data set (22.1%). Owing to the small size of each data set, the spread in the wind direction was limited. a, p, max S, and σ all followed the same basic trend, though max S followed σ more closely and a followed p very closely. The peak in B for daytime on 13 May was associated with decreases in the other four metrics and marked a decrease in variation in wind speed. μ tended to skew negative at night, but was otherwise negligible. a had a daytime mean and standard deviation of 0.0035185 and 0.0036348, and a nighttime mean and standard deviation of 0.0055622 and 0.0048156, respectively. p had a daytime mean and standard deviation of −1.5874 and 0.12869 and a nighttime mean and standard deviation of −1.7058 and 0.043115, respectively. p ranged between −1.4 and −1.8, with a notable outlier of −1.4 in the daytime on 14 May.

There was no apparent cyclical pattern in $log\ a$, p, max S, and σ, as might be expected from the diurnal cycle. This runs counter to the common understanding that winds are less turbulent at night due to a lack of surface heating [49]. However, the significant change in these spread parameters between the daytime and nighttime on 13 July demonstrates that the wind spectrum can vary dramatically on the diurnal time scale. The negative skew of μ and the smaller size of usable U_{data} reflect that the prevailing wind direction reversed for the nighttime 12 and 15 May data sets. The value of p agreed well with the Kolmogorov −5/3 law, with some minor variations on the diurnal time scale.

4.4. Seasonal Results and Discussion

At least 50% of data of all 7-day data sets satisfied the conditions for U_{data}, except for the August data set (49.4%). It was assumed that this had a negligible impact on the results. a, p, and max S all followed one another closely, with apparent maxima in May and August and minima in January and October. μ skewed positive in July, but was otherwise negligible. a had a mean and standard deviation of 0.0057547 and 0.0025145. p had a mean and standard deviation of -1.6238 and 0.097902. p ranged between -1.3 and -1.7, with a notable outlier of -1.35 in January.

There was an oscillating pattern in spread parameters from March to November. Seasonal local maxima in a and p occurred at the end of each season, and seasonal local maxima in B occurred in the middle of each season. The value of p agreed well with the Kolmogorov $-5/3$ law, with some minor variations on the seasonal time scale.

4.5. Interannual Results and Discussion

At least 50% of the data of all 7-day data sets satisfied the conditions for U_{data}, except for the 2016 data set (33.2%) and the 2017 data set (44.0%). The distribution of wind direction in 2012 and 2016 was sharply bimodal. a, p, and max S decreased in the years of 2016–2019, but increased again in the years of 2020–2021. This trend was reversed in σ and not apparent in B. μ skewed negative in 2015 and positive in 2018, but was otherwise negligible. a had a mean and standard deviation of 0.0082491 and 0.0036427, respectively. p had a mean and standard deviation of -1.6411 and 0.063125, respectively. p ranged between -1.4 and -1.8.

While there was a clear change in the spectrum in the years of 2016–2019 and again in 2020–2021, the driving mechanism behind this change is unclear. The influence of interannual meteorological cycles, such as El Niño, or changes in human factors due to the COVID-19 pandemic are questionable at best and would require further exploration. As interannual data sets were only taken from the month of May, there may be other interannual trends that were not identified in this work. The value of p agreed well with the Kolmogorov $-5/3$ law, with a notable outlier of -1.45 in 2020.

5. Conclusions

To better inform advanced control strategies and modeling efforts in the field of wind energy, a study on the dependence of the wind spectrum on wind speed and large time scales was conducted using data collected from the Eolos wind research station in Minnesota. Frequency analysis of wind samples with similar mean velocities showed that the low-frequency spectral content of wind speed fell off as wind speed increased. The location of high-frequency spectral peaks tended toward higher frequencies as the wind speed increased. These trends became more apparent as the number of samples increased.

Frequency analyses of wind subsets across diurnal, seasonal, and interannual time scales were conducted to identify trends in the wind spectrum over time. Power law approximations of the spectra were presented with time-varying parameters. While there was no apparent cyclical pattern in the spectrum over the diurnal cycle, sharp changes in the spectrum over one night demonstrated that the wind spectrum could vary dramatically at a time scale on the order of one day. There was an oscillating pattern in the spectrum on a seasonal time scale, with high-frequency variability rising at the end of each season and a significant increase from winter to spring. This behavior suggested that high-frequency variability increased during weather transition periods. There was a clear decrease in high-frequency variability in the years 2016–2019 when considering the interannual time scale. The mechanism behind this change is unclear. As data sets for the interannual time scale were all taken from the month of May, there may be other interannual trends not identified in this work. The Kolmogorov $-5/3$ law was observed across all three data batches, but variations in slope of up to 0.3 were observed across all three time scales. Future work might consider the spectrum of wind in the wake of the turbine, which would be especially relevant in the control and optimization of wind turbine arrays.

Author Contributions: Conceptualization, N.G., B.M. and K.A.S.; methodology, N.G. and B.M.; software, N.G.; formal analysis, N.G.; investigation, N.G.; resources, N.G.; data curation, N.G.; writing—original draft preparation, N.G.; writing—review and editing, N.G., B.M. and K.A.S.;

visualization, N.G.; supervision, K.A.S.; project administration, K.A.S. All authors have read and agreed to the published version of the manuscript.

Funding: This research received no external funding.

Institutional Review Board Statement: Not applicable.

Informed Consent Statement: Not applicable.

Data Availability Statement: Data were obtained from the Eolos wind research station, part of the St. Anthony Falls Laboratory at the University of Minnesota, and are available from https://eolos.umn.edu/contact (accessed on 2 February 2023) on request.

Acknowledgments: The authors thank the following members of the Hydraulic Power Transmission Laboratory at the University of Minnesota for their help with this research: Justin Chen, Daniel Escobar, Mike Gust, Mark Leinberger, Luuk Rousseau, and Yingkun Shen. The authors would also like to thank researchers from the Fluid Mechanics Laboratory and the St. Anthony Falls Laboratory: Lian Shen, Anqing Xuan, and Tianyi Li for background information and review, Chris Feist for help with data collection, and the Eolos wind energy group.

Conflicts of Interest: The authors declare no conflict of interest.

References

1. Manwell, J.F.; McGowan, J.G.; Rogers, A.L. *Wind Energy Explained: Theory, Design and Application*, 2nd ed.; Wiley: Chichester, UK, 2009; ISBN 978-0-470-01500-1.
2. Richardson, L. *Weather Prediction by Numerical Process*; Cambridge University Press: Cambridge, UK, 1922.
3. Kolmogorov, A. Dissipation of Energy in the Locally Isotropic Turbulence. *Proc. R. Soc. Lond. Ser. Math. Phys. Sci.* **1941**, *434*, 15–17. [CrossRef]
4. Kaimal, J.C.; Wyngaard, J.C.; Izumi, Y.; Coté, O.R. Spectral Characteristics of Surface-Layer Turbulence. *Q. J. R. Meteorol. Soc.* **1972**, *98*, 563–589. [CrossRef]
5. Grant, H.L.; Stewart, R.W.; Moilliet, A. Turbulence Spectra from a Tidal Channel. *J. Fluid Mech.* **1962**, *12*, 241. [CrossRef]
6. Högström, U. Review of Some Basic Characteristics of the Atmospheric Surface Layer. *Bound. Layer Meteorol.* **1996**, *78*, 215–246. [CrossRef]
7. Rosenberg, B.J.; Hultmark, M.; Vallikivi, M.; Bailey, S.C.C.; Smits, A.J. Turbulence Spectra in Smooth- and Rough-Wall Pipe Flow at Extreme Reynolds Numbers. *J. Fluid Mech.* **2013**, *731*, 46–63. [CrossRef]
8. Van der Hoven, I. Power Spectrum of Horizontal Wind Speed in the Frequency Range from 0.0007 to 900 Cycles per Hour. *J. Meteorol.* **1957**, *14*, 160–164. [CrossRef]
9. Orlanski, I. Rational Subdivision of Scales for Atmospheric Processes. *Bull. Am. Meteorol. Soc.* **1975**, *56*, 527–530.
10. Pielke, R.A. *Mesoscale Meteorological Modeling*, 3rd ed.; Academic Press: Cambridge, MA, USA; Elsevier: Amsterdam, The Netherlands, 2013; Volume 98, pp. 1–726. ISBN 978-0-12-385238-0.
11. Stull, R.B. *An Introduction to Boundary Layer Meteorology*; Springer: Berlin/Heidelberg, Germany, 2003; ISBN 978-94-009-3027-8.
12. Thunis, P.; Bornstein, R. Hierarchy of Mesoscale Flow Assumptions and Equations. *J. Atmos. Sci.* **1996**, *53*, 380–397. [CrossRef]
13. Davenport, A.G. The Spectrum of Horizontal Gustiness near the Ground in High Winds. *Q. J. R. Meteorol. Soc.* **1961**, *87*, 194–211. [CrossRef]
14. MacCready, P.B., Jr. The Inertial Subrange of Atmospheric Turbulence. *J. Geophys. Res.* **1962**, *67*, 1051–1059. [CrossRef]
15. Payne, F.R.; Lumley, J.L. One-Dimensional Spectra Derived from an Airborne Hot-Wire Anemometer. *Q. J. R. Meteorol. Soc.* **1966**, *92*, 397–401. [CrossRef]
16. Högström, U.; Hunt, J.C.R.; Smedman, A.-S. Theory and Measurements for Turbulence Spectra and Variances in the Atmospheric Neutral Surface Layer. *Bound. Layer Meteorol.* **2002**, *103*, 101–124. [CrossRef]
17. Larsén, X.G.; Larsen, S.E.; Petersen, E.L. Full-Scale Spectrum of Boundary-Layer Winds. *Bound. Layer Meteorol.* **2016**, *159*, 349–371. [CrossRef]
18. Ortiz-Suslow, D.G.; Wang, Q. An Evaluation of Kolmogorov's $-5/3$ Power Law Observed Within the Turbulent Airflow Above the Ocean. *Geophys. Res. Lett.* **2019**, *46*, 14901–14911. [CrossRef]
19. Pao, L.Y.; Johnson, K.E. Control of Wind Turbines. *IEEE Control Syst. Mag.* **2011**, *31*, 44–62. [CrossRef]
20. Xiao, Y.; Li, Y.; Rotea, M.A. CART3 Field Tests for Wind Turbine Region-2 Operation with Extremum Seeking Controllers. *IEEE Trans. Control Syst. Technol.* **2019**, *27*, 1744–1752. [CrossRef]
21. Krstić, M. Performance Improvement and Limitations in Extremum Seeking Control. *Syst. Control Lett.* **2000**, *39*, 313–326. [CrossRef]
22. Kumar, D.; Chatterjee, K. A Review of Conventional and Advanced MPPT Algorithms for Wind Energy Systems. *Renew. Sustain. Energy Rev.* **2016**, *55*, 957–970. [CrossRef]
23. Pande, J.; Nasikkar, P.; Kotecha, K.; Varadarajan, V. A Review of Maximum Power Point Tracking Algorithms for Wind Energy Conversion Systems. *J. Mar. Sci. Eng.* **2021**, *9*, 1187. [CrossRef]

24. Ghaffari, A.; Krstić, M.; Seshagiri, S. Power Optimization and Control in Wind Energy Conversion Systems Using Extremum Seeking. *IEEE Trans. Control Syst. Technol.* **2014**, *22*, 1684–1695. [CrossRef]
25. Creaby, J.; Li, Y.; Seem, J.E. Maximizing Wind Turbine Energy Capture Using Multivariable Extremum Seeking Control. *Wind Eng.* **2009**, *33*, 361–387. [CrossRef]
26. Mohr, E.; Mohanty, B.; Escobar-Naranjo, D.; Stelson, K.A. *Experimentation on a Hydraulic Energy Storage System for Mid-Size Wind Turbines*; American Society of Mechanical Engineers Digital Collection: New York, NY, USA, 2021.
27. Escobar-Naranjo, D.; Mohanty, B.; Stelson, K.A. *Experimental Validation of Extremum Seeking Control for a Midsize Hydrostatic Transmission Wind Turbine*; American Society of Mechanical Engineers Digital Collection: New York, NY, USA, 2022.
28. Mohanty, B.; Stelson, K.A. Experimental Validation of a Hydrostatic Transmission for Community Wind Turbines. *Energies* **2022**, *15*, 376. [CrossRef]
29. Leinberger, M. *Analysis and Simulation to Understand the Dynamics and Control of a Hydrostatic Wind Turbine*; American Society of Mechanical Engineers: Sarasota, FL, USA, 2023.
30. Musial, W.; Hitt, C.C.; Sloan, C.; Pilot, J.; Groenveld, K. Research and Development Roadmap 3.0; National Offshore Wind Research & Development Consortium. 2021. Available online: https://nationaloffshorewind.org/wp-content/uploads/Roadmap-3.0-June-30-2021.pdf (accessed on 17 October 2022).
31. OpenFAST Documentation 2022. Available online: https://www.nrel.gov/wind/nwtc/openfast.html (accessed on 10 March 2023).
32. Marten, D. *QBlade: A Modern Tool for the Aeroelastic Simulation of Wind Turbines*; Technische Universität Berlin: Berlin, Germany, 2020.
33. Jonkman, B.J. Turbsim User's Guide: Version 1.50. 2009. Available online: https://www.nrel.gov/docs/fy09osti/46198.pdf (accessed on 10 March 2023).
34. IEC. *Design Requirements: = Exigences de Conception; Wind Turbines*, 3rd ed.; Internationale Elektrotechnische Kommission, Ed.; IEC: Geneva, Switzerland, 2005; ISBN 978-2-8318-8161-4.
35. Stone, N. EOLOS Educational Data Set: An Overview. Available online: http://eolos.umn.edu/sites/eolos.dl.umn.edu/files/general/eolos_educational_data_set.pdf (accessed on 17 October 2022).
36. Li, J.; Abraham, A.; Guala, M.; Hong, J. Evidence of Preferential Sweeping during Snow Settling in Atmospheric Turbulence. *J. Fluid Mech.* **2021**, *928*, A8. [CrossRef]
37. Gao, L.; Li, B.; Hong, J. Effect of Wind Veer on Wind Turbine Power Generation. *Phys. Fluids* **2021**, *33*, 015101. [CrossRef]
38. Gao, L.; Yang, S.; Abraham, A.; Hong, J. Effects of Inflow Turbulence on Structural Response of Wind Turbine Blades. *J. Wind Eng. Ind. Aerodyn.* **2020**, *199*, 104137. [CrossRef]
39. Hong, J.; Abraham, A. Snow-Powered Research on Utility-Scale Wind Turbine Flows. *Acta Mech. Sin.* **2020**, *36*, 339–355. [CrossRef]
40. Abraham, A.; Dasari, T.; Hong, J. Investigation of the Near-Wake Behaviour of a Utility-Scale Wind Turbine. *J. Phys. Conf. Ser.* **2020**, *1452*, 012067. [CrossRef]
41. Dasari, T.; Wu, Y.; Liu, Y.; Hong, J. Near-Wake Behaviour of a Utility-Scale Wind Turbine. *J. Fluid Mech.* **2019**, *859*, 204–246. [CrossRef]
42. Howard, K.B.; Guala, M. Upwind Preview to a Horizontal Axis Wind Turbine: A Wind Tunnel and Field-Scale Study. *Wind Energy* **2016**, *19*, 1371–1389. [CrossRef]
43. Chamorro, L.P.; Lee, S.-J.; Olsen, D.; Milliren, C.; Marr, J.; Arndt, R.E.A.; Sotiropoulos, F. Turbulence Effects on a Full-Scale 2.5 MW Horizontal-Axis Wind Turbine under Neutrally Stratified Conditions: Turbulence Effects on a Full-Scale Wind Turbine. *Wind Energy* **2015**, *18*, 339–349. [CrossRef]
44. Hong, J.; Toloui, M.; Chamorro, L.P.; Guala, M.; Howard, K.; Riley, S.; Tucker, J.; Sotiropoulos, F. Natural Snowfall Reveals Large-Scale Flow Structures in the Wake of a 2.5-MW Wind Turbine. *Nat. Commun.* **2014**, *5*, 4216. [CrossRef] [PubMed]
45. Hong, J.; Guala, M.; Chamorro, L.P.; Sotiropoulos, F. Probing Wind-Turbine/Atmosphere Interactions at Utility Scale: Novel Insights from the EOLOS Wind Energy Research Station. *J. Phys. Conf. Ser.* **2014**, *524*, 012001. [CrossRef]
46. Clipper Windpower. Liberty 2.5 MW Wind Turbine 2009. Available online: https://geosci.uchicago.edu/~moyer/GEOS24705/Readings/Liberty_Brochure_2009_LR.pdf (accessed on 17 October 2022).
47. Lim, K. *Settling Velocity of Snow with Varying Morphology in the Atmospheric Turbulence*; University of Minnesota: Minneapolis, MN, USA, 2020.
48. Yang, X.; Milliren, C.; Kistner, M.; Hogg, C.; Marr, J.; Shen, L.; Sotiropoulos, F. High-Fidelity Simulations and Field Measurements for Characterizing Wind Fields in a Utility-Scale Wind Farm. *Appl. Energy* **2021**, *281*, 116115. [CrossRef]
49. Prevailing Winds. Available online: https://www.weather.gov/source/zhu/ZHU_Training_Page/winds/Wx_Terms/Flight_Environment.htm (accessed on 27 November 2022).